arXiv:1201.4389v1 [astro-ph.HE] 20 Jan 2012

TIDAL DISRUPTIONS OF WHITE DWARFS FROM ULTRA-CLOSE ENCOUNTERS WITH INTERMEDIATE MASS SPINNING BLACK HOLES

Roland Haas[1,2], Roman V. Shcherbakov[3], Tanja Bode[1], Pablo Laguna[1]
Draft version January 24, 2012

ABSTRACT

We present numerical relativity results of tidal disruptions of white dwarfs from ultra-close encounters with a spinning, intermediate mass black hole. These encounters require a full general relativistic treatment of gravity. We show that the disruption process and prompt accretion of the debris strongly depend on the magnitude and orientation of the black hole spin. However, the late-time accretion onto the black hole follows the same decay, $\dot{M} \propto t^{-5/3}$, estimated from Newtonian gravity disruption studies. We compute the spectrum of the disk formed from the fallback material using a slim disk model. The disk spectrum peaks in the soft X-rays and sustains Eddington luminosity for $1-3$ yrs after the disruption. For arbitrary black hole spin orientations, the disrupted material is scattered away from the orbital plane by relativistic frame dragging, which often leads to obscuration of the inner fallback disk by the outflowing debris. The disruption events also yield bursts of gravitational radiation with characteristic frequencies of ~ 3.2 Hz and strain amplitudes of $\sim 10^{-18}$ for galactic intermediate mass black holes. The optimistic rate of considered ultra-close disruptions is consistent with no sources found in ROSAT all-sky survey. The future missions like Wide-Field X-ray Telescope (WFXT) could observe dozens of events.

Subject headings: accretion – black hole physics – gravitational waves – hydrodynamics – relativity – radiation mechanisms: general – X-rays: bursts

1. INTRODUCTION

Tidal disruptions of stars by black holes (BHs) are fascinating and violent cosmic events, releasing copious amounts of energy in electromagnetic radiation and, in some cases, also accompanied by potentially detectable gravitational wave emission. The scattered debris from a stellar disruption will yield different radiation patterns depending on the orientation of the orbit. This variety of radiation patterns will provide clues about both the BH and the internal structure of the disrupted star. As the debris from a tidal disruption showers back into the BH to form an accretion disk, for instance, it will radiate close to or above the Eddington luminosity for some duration, with the spectrum peaking at UV/X-ray frequencies depending on the BH mass (Rees 1988; Evans & Kochanek 1989; Cannizzo et al. 1990; Bogdanović et al. 2004; Strubbe & Quataert 2009). In addition, the unbound debris will quickly scatter over a large volume, and may be illuminated by the accretion disk, leading to an optical irradiation spectrum dominated by lines (Bogdanović et al. 2004; Sesana et al. 2008; Strubbe & Quataert 2009; Clausen & Eracleous 2011).

When a main sequence star is disrupted, the super-Eddington outflow is by itself hot enough to be a significant source of optical emission resembling supernova radiation (Kasen & Ramirez-Ruiz 2009; Strubbe & Quataert 2009). In these circumstances, instead of outflowing debris, a steady optically thick envelope may reprocess the inner disk radiation (Loeb & Ulmer 1997; Ulmer et al. 1998). As a consequence, neither the inner disk nor the irradiated debris emission is visible. Another tidal disruption effect arises from the tidal compression perpendicular to the orbital plane. The compression leads to the formation of a strong shock that triggers a powerful short outburst (Kobayashi et al. 2004; Guillochon et al. 2009; Rosswog et al. 2009). In some instances, e.g. ultra-close disruptions, the tidal compression could be strong enough to produce a thermonuclear ignition of the star. In such cases, the detonation of the star would be observed as an under-luminous supernova (Rosswog et al. 2009).

The variety of proposed radiative signatures often disagree with each other, calling for precise dynamical modeling of tidal disruptions. Early hydrodynamic simulations by Evans & Kochanek (1989) confirmed a flat distribution of debris mass over its energy range, yielding the predicted $t^{-5/3}$ law of fallback accretion rate (Rees 1988). Other numerical investigations addressed the tidal compression and related shock formation; some of these studies used smoothed particle hydrodynamics (SPH) techniques (Kobayashi et al. 2004; Rosswog et al. 2009) and others hydrodynamic grid-based codes (Guillochon et al. 2009). The studies by Rosswog et al. (2009) included nuclear reactions with simplified networks. On the other hand, Bogdanović et al. (2004) looked at the formation of spherical envelopes Loeb & Ulmer (1997) using SPH simulations, but the study did not find any conclusive evidence of a spherical structure. At present tidal disruption simulations that capture all the relevant physics are quite challenging. The simulations require handling, in addition to hydrodynamics, effects from general relativity, nuclear reactions, and magnetic fields. Thus, many important questions are still left unanswered. In particular, there are very few simulations that account for general relativistic effects (Laguna et al. 1993a,b; Kobayashi et al. 2004; Bogdanović et al. 2004). The inclusion of magnetic fields may lead to jet formation.

Very likely, the BHs involved in a tidal disruption will have spins misaligned with the orbital angular momentum of the

[1] Center for Relativistic Astrophysics, School of Physics, Georgia Institute of Technology, Atlanta, GA 30332, USA
[2] Theoretical AstroPhysics Including Relativity, California Institute of Technology, Pasadena, CA 91125, USA
[3] Hubble Fellow, Department of Astronomy, University of Maryland, College Park, MD 20742-2421, USA

incoming star. Thus the disk formed from the tidal debris will have angular momentum that is also misaligned with the BH spin direction (Rees 1988). For thin disks, the Bardeen-Petterson effect will align the BH spin with the angular momentum of the inner region of the disk (Bardeen & Petterson 1975), but for the thick disks expected from tidal disruptions, the alignment may not happen (Papaloizou & Pringle 1983; Fragile et al. 2007; Stone & Loeb 2011). This misalignment could have important consequences on the emission channels from the disruption, e.g. jet formation. The spin of the BH will also produce distinct effects in an ultra-close encounter, when the pericentric radius $R_{\rm p}$ is comparable to the gravitational radius $R_{\rm g} = GM_{\rm bh}/c^2$ of the BH. In this strong gravity regime, the details of the disruption will depend not only on the stellar radius, stellar equation of state, and orbital energy, but also on the magnitude and orientation of the spin of the BH. In particular, the properties of the accretion will depend on the BH spin since its magnitude determines the location of the innermost stable circular orbit (ISCO) radius $r_{\rm ISCO}$, ranging from $r_{\rm ISCO} = 9R_{\rm g}$ for a counter-rotating maximally spinning BH to $r_{\rm ISCO} = 1R_{\rm g}$ for a co-rotating maximally spinning BH. The value of spin determines whether the star following the same orbit gets disrupted (Kesden 2011). Furthermore, a misaligned rotating BH will drag around nearby debris (Bardeen et al. 1972; Shapiro & Teukolsky 1986), and will effectively push this material away from the orbital disruption plane. The net effect will be the formation of a shell-like disruption debris engulfing the BH, as opposed to the traditional S-shape debris observed in Newtonian gravity simulations (Evans & Kochanek 1989).

The present work aims at exploring the exciting regime of ultra-close encounters (i.e. $R_{\rm p} \sim$ few $R_{\rm g}$) of a white dwarf (WD) with an intermediate mass black hole (IMBH). Our main goal is to investigate observational signatures due to strong gravity effects that may shed light on the presence of IMBHs. We consider a carbon-oxygen WD with mass $M_{\rm wd} = 1 M_\odot$ and radius (Nauenberg 1972)

$$R_{\rm wd} = 1.56 R_\oplus \left(\frac{M_{\rm wd}}{M_{\rm ch}}\right)^{-1/3} \left[1 - \left(\frac{M_{\rm wd}}{M_{\rm ch}}\right)^{4/3}\right]^{3/4}$$
$$= 0.86 R_\oplus \qquad (1)$$

with $M_{\rm ch} = 1.44 M_\odot$ the Chandrasekhar mass and $R_\oplus = 6,960$ km the Earth mean radius. We fix the mass of the IMBH to $M_{\rm bh} = 10^3 M_\odot$. With these choices, $R_{\rm wd} \simeq 4 R_{\rm g} \simeq 6,000$ km. Therefore, the WD and IMBH can be numerically modeled with comparable grid resolutions. The other important scale in the problem is the tidal disruption radius R_t. For our setup (Rees 1988),

$$\frac{R_{\rm t}}{R_{\rm g}} \simeq 40 \left(\frac{R_{\rm wd}}{0.86 R_\oplus}\right) \left(\frac{M_{\rm wd}}{1 M_\odot}\right)^{-1/3} \left(\frac{M_{\rm bh}}{10^3 M_\odot}\right)^{-2/3}, \quad (2)$$

gave us ample room to carry out deep penetration encounters.

Currently, there is a large body of evidence for the existence of both solar mass as well as supermassive BHs with masses in the range of $10^5 - 10^8 M_\odot$. IMBHs are, however, the missing link between stellar mass and supermassive BHs. Today, only tentative evidence exists (Irwin et al. 2010; Farrell et al. 2009; Davis et al. 2011). On the other hand, WDs are thought to be abundant in spiral galaxies (Evans et al. 1987; Reid 2005) and globular clusters (Gerssen et al. 2002). Thus the identification of distinct signals in both gravitational waves

(GWs) and the electromagnetic spectrum (Gould 2011) from a disruption event could potentially guide observations that provide evidence for the existence of IMBH as well as insights into the structure of the WD involved.

Our study uses the full machinery of numerical relativity to solve the Einstein equations of general relativity and hydrodynamics. We do not include nuclear reactions. For the ultra-close encounters of our interest, with $R_{\rm p} \sim$ few $R_{\rm g}$, a general relativistic description of gravity is needed. However, given the mass ratio $M_{\rm wd}/M_{\rm bh} \simeq 10^{-3}$ of the bodies involved and encounters not driven by GW emission, one does not need to account for dynamical general relativistic gravity. The present study could have been carried out by doing hydrodynamics on the fixed space-time background provided by the IMBH. However, this would have implied developing a general relativistic hydro code on a fixed background, a code similar to the SPH code developed by one of us to investigate the tidal disruption of main sequence stars by supermassive BHs (Laguna et al. 1993a,b). We decided instead to take advantage of our numerical relativity code MAYA. The code has demonstrated excellent performance in handling fluid flows in the vicinity of BHs in our studies of binary BH mergers in astrophysical environments (Bode et al. 2008; Bode et al. 2009; Bode et al. 2011). The other advantage of using the MAYA code is the ability to obtain the GW signal directly from the simulation, without having to take recourse to the possibly inaccurate quadrupole formula or the application of post Newtonian (PN) approximations to space-times containing a spinning BH.

The paper is organized as follows. In § 2, we describe how self-consistent general relativistic initial data is constructed. Results from the dynamics of the disruption events are discussed in § 3. We estimate electromagnetic transient radiation in § 4 using a slim disk model to compute the spectrum during the fallback phase. We find that the sources shine at Eddington luminosity $\sim 10^{41} {\rm erg \ s^{-1}}$ for about $1-3$ yrs, and then fade approximately as $\propto t^{-5/3}$. We also find that there is a 50/50 chance that the inner disk will be obscured by outflowing debris for a fully misaligned BH spin. In § 5, we calculate the gravitational wave signal produced during the encounters. In § 6 we estimate the event rates and discuss the observational prospects. We discuss the progress and the limitations of our study in § 7.

2. INITIAL DATA AND CODE TESTS

When using a fully general relativistic code, such as our MAYA code, that is based on a 3+1 formulation of the Einstein equations, the initial data for the dynamical space-time are comprised of the spatial metric γ_{ij} and the extrinsic curvature K_{ij} of the initial space-time hypersurface. All tensor indices are spatial indices and, in this section only, we use units for which $G = c = 1$. The metric γ_{ij} characterizes the gravitational potentials of the IMBH and WD, and the tensor K_{ij} provides the "velocity" of the metric, or the embedding of the spacelike hypersurface, in the space-time.[4]

Although γ_{ij} and K_{ij} are dominated by the IMBH, it is crucial to account for the contributions from the WD in order to correctly include the self-gravity of the WD. The components of γ_{ij} and K_{ij} cannot all be freely specifiable. They need to

---

[4] For a review on numerical relativity, we recommend the textbooks by Alcubierre (2008) and Baumgarte & Shapiro (2010)

satisfy the following elliptic equations

$$8\,\Delta\phi + \phi^{-5}\bar{A}_{ij}\bar{A}^{ij} = -16\pi\,\phi^{-3}\bar{\rho}_*, \tag{3}$$

$$\partial_j\bar{A}^{ij} = 8\pi\bar{J}^i, \tag{4}$$

where

$$\gamma_{ij} = \phi^4\delta_{ij} \tag{5}$$

$$K^{ij} = \bar{A}^{ij}\phi^{-10} \tag{6}$$

$$\rho_* = \bar{\rho}_*\phi^{-8} \tag{7}$$

$$J^i = \bar{J}^i\phi^{-10}. \tag{8}$$

Above, ϕ is a conformal factor, $\delta_{ij} = \mathrm{diag}(1,1,1)$ the flat spatial metric and Δ its associated Laplace operator. In writing Eqs. (3) and (4), we have made the customary assumption that the initial physical metric γ_{ij} is conformally flat and K_{ij} is trace-free. Eqs. (3) and (4) are, respectively, the conformal versions of the so-called Hamiltonian and momentum constraints of general relativity (York 1979). The sources ρ_* and J^i are, respectively, the total energy and momentum densities.

Our approach to solve the Hamiltonian and momentum constraints is to specify the "free" data in Eqs. (3) and (4) from the solutions to an isolated, spinning BH, and a boosted WD (Löffler et al. 2006).

Let us consider first the solution for a boosted WD. The sources $\bar{\rho}_*$ and $\bar{J}^i$ in Eqs. (3) and (4) are obtained from the stress-energy tensor for a perfect fluid (see chapter 5 in Baumgarte & Shapiro 2010). They read

$$\bar{\rho}_* = \rho\left(1+\varepsilon+\frac{P}{\rho}\right)W^2 - P, \tag{9}$$

$$\bar{J}^i = \rho\left(1+\varepsilon+\frac{P}{\rho}\right)W^2 v^i, \tag{10}$$

where $W = (1-\gamma_{ij}v^iv^j)^{-1/2}$ is the Lorentz factor and v^i the boost velocity of the WD. In (9) and (10), ρ is the rest-mass density, P the pressure, and ε the specific internal energy density. The values for those quantities are obtained from Tolman-Oppenheimer-Volkoff (TOV) solutions (Oppenheimer & Volkoff 1939; Tolman 1939) with a polytropic equation of state $P = K\rho^\Gamma$. We use $\Gamma = 5/3$ appropriate for a non-degenerate gas, which is sufficient to capture the dynamics during the inspiral and disruption phases. During the evolution, we switch to a gamma-law equation of state $P = \rho\varepsilon(\Gamma-1)$. We denote the solutions to Eqs. (3) and (4) in the absence of the BH by $\phi_{\rm wd}$ and $\bar{A}^{\rm wd}_{ij}$.

Now we consider the solution to the constraints for a spinning BH. In the absence of the WD, $\bar{\rho}_* = 0$ and $\bar{J}^i = 0$. In this case, the momentum constraint (4) can be solved analytically (Bowen & York 1980). The solution reads

$$\bar{A}^{\rm bh}_{ij} = \frac{3}{r^3}\left(\epsilon_{kil}S^l l^k l_j + \epsilon_{kjl}S^l l^k l_i\right) \tag{11}$$

with $l^i = x^i/r$ and ϵ_{ijk} the three-dimensional Levi-Civita symbol. Above, S^i is the spin vector of the BH.

With the solutions $\bar{A}^{\rm wd}_{ij}$ and $\bar{A}^{\rm bh}_{ij}$ at hand, it is clear that the linear superposition $\bar{A}_{ij} = \bar{A}^{\rm bh}_{ij} + \bar{A}^{\rm wd}_{ij}$ is the solution to the momentum constraint (4) in the presence of both a WD and a BH. Next, we solve the Hamiltonian constraint (4) with $\bar{A}_{ij} = \bar{A}^{\rm bh}_{ij} + \bar{A}^{\rm wd}_{ij}$ and $\bar{\rho}_*$ given by (9). We use the popular ansatz

$$\phi = 1 + \frac{M_{\rm bh}}{2r} + u. \tag{12}$$

Thus, equation (3) becomes an equation for u. In (12), the first term is the flat space solution to (3); the second is the BH solution; and the third term u includes both the gravitational potential of the WD as well as the interaction effects with the BH.

To test our initial data method, and in particular to assess the importance of the WD-BH interaction effects, we compute initial data for a WD initially at rest; that is, $\bar{J}^i = 0$ and thus $\bar{A}^{\rm wd}_{ij} = 0$. In addition, we assume a non-spinning BH, i.e. $\bar{A}^{\rm bh}_{ij} = 0$. The Hamiltonian constraint (3), with the help of (12), takes the form

$$\bar{\Delta}u = -16\pi\,\phi^{-3}\bar{\rho}_*. \tag{13}$$

The solution to (13) is shown in Figure 1. For color versions of the figures in this paper see the electronic edition of the Journal. Also in Figure 1 is the solution $u_{\rm wd}$ to equation (13) without the BH; that is, with $M_{\rm bh} = 0$ in (12). The difference between u and $u_{\rm wd}$ is entirely due to the gravitational interaction of the WD with the BH.
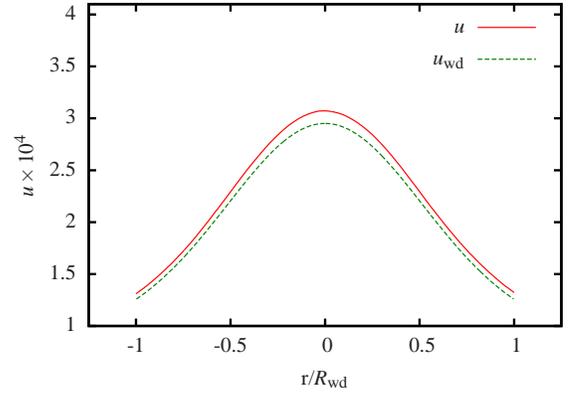
FIG. 1.— Solution u to equation (13) for a WD at rest a distance $15\,R_{\rm wd}$ away from a non-spinning IMBH. The solution u provides not only the gravitational potential of the WD but also includes the full non-linear interactions with the IMBH. For comparison, we plot also $u_{\rm wd}$, the solution to equation (13) for a WD in isolation.

We also tested the ability of our method to produce stable isolated WD models and to conserve rest mass. We found that, over six dynamical times, the central density of the WD did not change more than 1.2% of its initial value and rest mass was conserved at the 0.1% level. This is in spite of the adaptive mesh refinement infrastructure we use (CARPET) not being designed to accurately preserve rest mass conservation when interpolating between different refinement levels.

3. SIMULATION RESULTS

3.1. *Tidal Disruption Simulation Parameters*

Our study consists of a series of six simulations. As mentioned before, the IMBH has a mass $M_{\rm bh} = 10^3\,M_\odot$, and the WD has a mass $M_{\rm wd} = 1\,M_\odot$ and radius $R_{\rm wd} \simeq 6{,}000\,{\rm km}$ (Hamada & Salpeter 1961). The WD mass and radius correspond to a central density $\rho_{\rm initial} = 1.33\times10^7\,{\rm g\,cm^{-3}}$, $\Gamma = 5/3$, and polytropic constant $K = 2.41\times10^{-9}\,({\rm cm^3\,g^{-1}})^{\Gamma-1}$. All the simulations start with the WD in a parabolic orbit, in the Newtonian gravity sense, a distance $1.5R_{\rm t} \simeq 60R_{\rm g}$ along the negative $\hat{x}$-axis away from the IMBH. The orbital angular momentum of the WD is aligned with the $\hat{z}$-axis, as depicted in Figure 2.

Table 1 lists the configurations used in the simulations where $\beta = R_{\rm t}/R_{\rm p}$ is the penetration factor for an orbit with
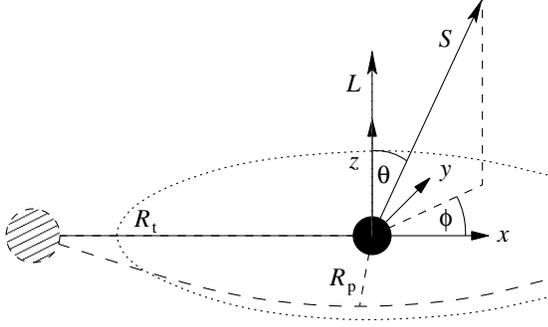
FIG. 2.— Configuration setup of our simulations. The WD is located a distance $1.5 R_t \simeq 60 R_g$ along the negative $\hat{x}$-axis away from the BH. The orbital angular momentum $\vec{L}$ of the WD is aligned with the $\hat{z}$-axis. The orientation of the BH spin $\vec{S}$ is determined by the standard θ and ϕ angles in a right handed spherical coordinate system.

pericentric distance R_p, and $a^\star = |\vec{S}|/M^2$ is the magnitude of the dimensionless spin parameter of the IMBH. The angles θ and ϕ determine the direction of the BH spin. They are the standard angles in a right-handed spherical coordinate system as depicted in Figure 2. We use the following convention to label the cases we studied. If a case is labeled "BxSy", the WD had penetration factor $\beta = x$. In addition, the value of y denotes a non-spinning BH (y=0) or the BH's spin orientation: (up, down, in-plane, arbitrary) for y = (u,d,i,a), respectively.

Run	β	$a^\star$	θ	ϕ
B6S0	6	0.0	0°	0°
B6Su	6	0.6	0°	0°
B6Sd	6	0.6	180°	0°
B6Si	6	0.6	90°	0°
B6Sa	6	0.6	63°	90°
B8Sa	8	0.6	63°	90°

TABLE 1
SIMULATION PARAMETERS: $\beta = R_t/R_p$ IS THE PENETRATION FACTOR, $a^\star = |\vec{S}|/M^2$ IS THE DIMENSIONLESS SPIN PARAMETER OF THE CENTRAL BLACK HOLE, θ AND ϕ ARE THE ANGLES BETWEEN $\vec{S}$ AND THE ORBITAL ANGULAR MOMENTUM ($\hat{z}$-AXIS) AND THE RADIAL DIRECTION JOINING THE IMBH AND THE WD ($\hat{x}$-AXIS), RESPECTIVELY.

In all the simulations, we employ eight levels of mesh refinement with radii $1.24 R_g \times 2^\ell$ ($0 \le \ell \le 7$) centered at the BH location. In addition to these refinement levels, we surround the WD during the pre-disruption phase with five additional nested boxes of radii $4.96 R_g \times 2^\ell$ ($0 \le \ell \le 4$). The resolution on the finest refinement is $R_g/19.35$, the resolution on the level covering the WD is $R_g/9.675$. This mesh refinement setup becomes insufficient when the WD begins to be disrupted. At this point, we turn off the boxes tracking the WD and construct a larger mesh with resolution $R_g/9.675$ that includes both the IMBH and the highly distorted WD. Once the expanding debris has cleared the inner region and the density has dropped, we turn off this level again to speed up the simulation.

The mesh refinements affect our ability to conserve rest mass throughout the computational domain, in particular if the meshes are moving, created, or removed. Figure 3 displays the relative gain/loss of rest mass in the computational domain, $\delta M/M_{wd} = (M - M_{wd})/M_{wd}$, where M is the total relativistic rest mass and M_{wd} the initial WD rest mass. The computed value of M takes into account the mass loss through the BH horizon and the outer boundary of the computational domain. We find tolerable mass conservation, with violations of

less than 4% over the course of the simulations. Runs B6Su and B6S0 display the worst mass conservation. As we shall see, these are the cases in which most of the material of the star ($\gtrsim 95\%$) escapes the BH, forming an expanding cloud that reaches the coarsest mesh refinements. Notice also that most of the errors in mass conservation accumulate after the disruption. Run B6Sd is the only run that loses mass. This is the case in which the IMBH accretes almost all of the star during the initial passage of the WD.
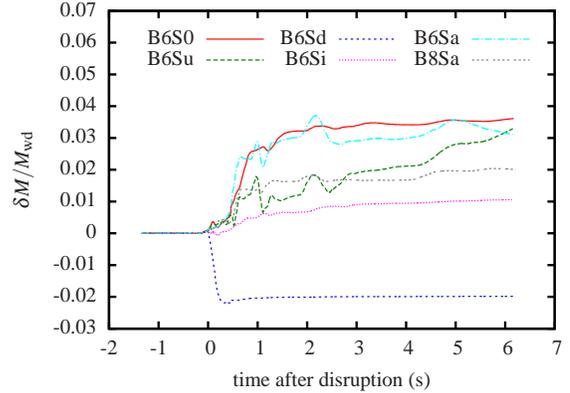
FIG. 3.— Relative gain/loss of rest mass in the computational domain, $\delta M/M_{wd} = (M - M_{wd})/M_{wd}$, where M is the total relativistic rest mass and M_{wd} the initial WD rest mass. The total relativistic rest mass M takes into account fluxes into the BH. The only simulation run displaying a net mass loss is the case B6Sd in which almost all the material accretes promptly. In the other cases, most of the mass gain happens in the short high compression phase when the WD is at its periapsis point close to the BH.

3.2. Tidal compression

The first stage in a tidal disruption encounter consists of the deformations that the incoming star experiences due to the tidal forces. In the orbital plane of the star, there are two competing tidal deformations. One of them is tidal stretching along the radial direction joining the IMBH with the WD. The other is tidal compression perpendicular to this radial direction. In the direction perpendicular to the orbital plane, there is also tidal compression. This compression, or squeezing, is stronger than that in the orbital plane because in the latter the radial direction changes rapidly as the star reaches periapsis, thus modifying the "contact point" in the star of the in-plane compression. We concentrate here on the compression in the direction perpendicular to the orbital plane. This compression could, in principle, generate enough heat to detonate the star (Luminet 1985; Luminet & Marck 1985; Luminet & Pichon 1989) by igniting nuclear reactions at the core of the WD (Rosswog et al. 2009). To investigate whether a nuclear ignition is likely to happen from tidal compression, we plot in Figure 4 the instantaneous maximum temperature of the star as a function of the density at that location. To a good approximation, this density is also the instantaneous maximum density. The instantaneous maximum temperature is computed as the mass-density-weighted temperature average of the portion of the star whose numerical cells that have the largest internal energy and make up for 10% of its mass.

We calculate temperatures T from the thermal specific energy as (see Lee et al. (2005))

$$m_p n_{nuc} \varepsilon_{th} = \frac{3}{2} k_B T (N_{ion} + N_e) n_{nuc} + a_{BB} T^4, \quad (14)$$
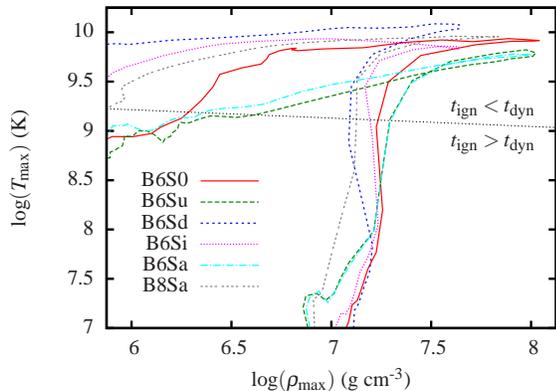
FIG. 4.— Instantaneous maximum temperature as a function of the density at the same location. We compute the density-weighted temperature average of the hottest cells in the grid which make up 10% of the total rest mass of the WD. The dotted black line separates regions in parameter space where the ignition time as estimated from Figure 2 of Dursi & Timmes (2006) is larger/smaller than the dynamical timescale of the WD, i.e. the region of successful explosion from the region where the explosion fails. Densities smaller than 10^7 g cm^{-3} are not present in Figure 2 and the estimates for the ignition time in this region are based on simple linear extrapolation. In all cases investigated, the ignition timescale t_{ign} of the WD is much shorter than the dynamical timescale $t_{dyn} = 1/\sqrt{G\rho} \gtrsim 0.38$ s of the WD.

with

$$\varepsilon_{th} = \varepsilon - \frac{K_{initial}}{\Gamma - 1} \rho^{\Gamma - 1}, \qquad (15)$$

where the second term in equation (15) is the "cold" specific internal energy in the absence of shocks. N_e is the number of electrons per nucleon making up the gas, N_{ion} is the number of ions per nucleon, n_{nuc} is the number density of nucleons in the gas, m_p is the proton (nucleon) mass, k_B is the Boltzmann constant, and a_{BB} here is the radiation constant. For simplicity we assume $N_{ion} = 1/14$, for an equal mixture of oxygen and carbon atoms. For N_e, which depends on the ionization state of the plasma, we use $N_e = 0$ for $T \lesssim 5 \times 10^6$ K and $N_e = 1/2$ for 5×10^6 K $\lesssim T \lesssim 1 \times 10^{10}$ K. That is, we ignore any partial ionization states of the constituent atoms at low temperatures.

In all cases investigated, the maximum temperature and density displayed in the tracks of Figure 4 reach high enough values to trigger nuclear burning in the star (cf. Figure 2 of Dursi & Timmes (2006)). Interestingly, the temperature-density tracks in Figure 4 are qualitatively similar to those by Rosswog et al. (2009), who included nuclear networks.

Run	β^*	T_{max} (10^9 K)	$\rho_{max}/\rho_{initial}$	f_{acc}	f_{unb}
B6S0	8.9	8.6	7.5	68%	19%
B6Su	9.44	6.6	9.3	< 1%	60%
B6Sd	11	12	3.2	> 99%	< 0.5%
B6Si	7.6	8.6	3.3	65%	22%
B6Sa	9.1	6.0	8.1	2%	67%
B8Sa	10	9.1	4.0	43%	34%

TABLE 2
ACTUAL PENETRATION FACTOR β^* MEASURED FROM THE SIMULATIONS. MAXIMUM TEMPERATURE T_{max} AND COMPRESSION $\rho/\rho_{INITIAL}$ WITH $\rho_{INITIAL} = 1.33 \times 10^7$ g cm^{-3}. FRACTION f_{ACC} OF THE STAR ACCRETED DURING THE FIRST 2s AFTER DISRUPTION, UNBOUND FRACTION f_{UNB} AT THE END OF THE SIMULATION AT $\sim$ 6s.

In Table 2, we list the maximum temperature T_{max} and compression $\rho_{max}/\rho_{initial}$. Here T_{max} and ρ_{max} are the maximum temperature and density attained over the course of the evolution. We also list the "actual" penetration factor

$\beta^* = R_t/R_p^*$. Recall that the orbital parameters, and in particular R_p, used to set the WD in a parabolic orbit were obtained using Newtonian gravity. Because of relativistic effects, the value of R_p^* will differ from the Newtonian estimate R_p, and thus $\beta \neq \beta^*$. In our simulations, we define R_p^* as the distance of closest approach of the point within the WD where T_{max}, or equivalently ρ_{max}, is found. Notice that for the B6Su and B6Sd cases, T_{max} almost doubles and ρ_{max} triples when going from a spin aligned with the orbital angular momentum to one that is anti-aligned. This is because in the anti-aligned case (B6Sd), the WD penetrates closer, $\beta^* = 11$, than in the aligned case (B6Sd), $\beta^* = 9.4$. Figure 5 shows the maximum temperature T_{max} and maximum density ρ_{max} as a function of the actual penetration factor β^* from Table 2. Because of the small range of values covered by β^*, it is not possible to verify the scaling $T_{max} \propto \beta^2$ and $\rho_{max} \propto \beta^3$ suggested by Carter & Luminet (1982)
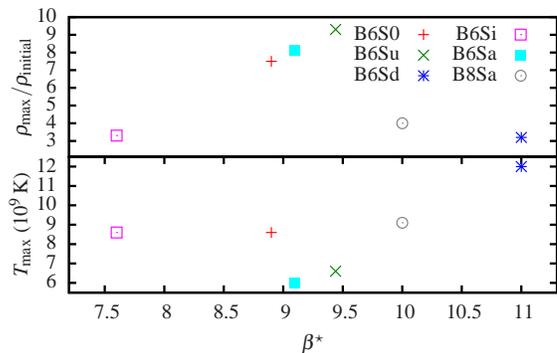
FIG. 5.— Maximum density ρ_{max} (top) and temperature T_{max} as a function of β^* for the values in Table 2.

3.3. Outflowing debris and spin

All cases showed that the mass and orientation of the debris after disruption is strongly affected by the BH spin. This is because the spin determines the location of ISCO radius, and it is also responsible for frame-dragging effects. In particular, frame-dragging pulls the material out of the orbital plane, thereby changing the orientation of the resulting disk.

We first discuss three disruptions: disruption by a non-spinning IMBH (case B6S0), by an IMBH with spin aligned (case B6Su), and by an IMBH with spin anti-aligned (case B6Sd) relative to the orbital angular momentum (see Table 2). For the spinning BH cases, the magnitude of the dimensionless spin parameter a^* was kept at 0.6. With this spin magnitude, $r_{ISCO} = 5,670$ km for the case B6Su, and $r_{ISCO} = 11,600$ km for the case B6Sd. In the non-spinning case, $r_{ISCO} = 9,000$ km (McClintock et al. 2011). All three cases had penetration factors $\beta = R_t/R_p = 6$. From equation (2), $R_t = 40R_g = 60,000$ km, thus a penetration factor of 6 translates to a pericentric distance $R_p \simeq 10,000$ km. We then expect that the WD in the retrograde case B6Sd will pass within the ISCO; in the prograde case B6Su the star will mostly stay outside of the ISCO; and in the case B6S0 the WD will graze by the ISCO. Because $r_{ISCO} > R_p$ in the B6Sd case, almost all of the star is accreted by the BH soon after the disruption. For the cases B6S0 and B6Su, on the other hand, most of the stellar debris escapes direct capture, expanding away from the hole. The debris cloud has a shape resembling a thick circular arch. This arch-like cloud eventually closes up and forms a disk around the BH.

In all cases, the leading edge of the tidally-disrupted star wraps around the BH and crashes into the trailing material creating a hot region. For the B6Su, B6Sd and B6S0 cases, this hot region is mostly contained within the equatorial plane and moves outwards from the central region in the form of a spiraling disturbance in the debris disk, eventually appearing on the debris surface. Figure 6 shows snapshots in the orbital plane of the density (top row) and temperature (bottom row) for runs B6Si and B6Su. The snapshots in the left column are for the case B6Si ~ 0.5 seconds after disruption. The middle and right columns correspond to case B6Su ~ 0.5 seconds and ~ 5.9 seconds after disruption, respectively. In the aligned case B6Su, the hot region forms a spiral which moves outwards from the point where the leading edge of the WD intersected with the tail material. At late times this feature has been washed out. In run B6Si the hot region is much smaller; frame dragging by the BH has pulled material out of the plane into a shell surrounding the BH.

For the cases in which the spin of the BH is not aligned with the orbital angular momentum of the binary (i.e. B6Si, B6Sa and B8Sa cases), frame dragging is effectively able to wrap the debris material around the BH. This effect – which is not captured by Newtonian calculations – greatly changes the geometry of the debris, blanketing the central region with a shell-like cloud of gas. We will address the observational consequences of the material surrounding the BH in the next section. The effect of the misalignment is evident from Figure 6 in the remarkable differences of the spiral patterns observed between the left and middle snapshots at ~ 0.5 seconds after disruption. The left panels are for the B6Si case in which the BH spin direction is perpendicular to the orbital angular momentum. On the other hand, the middle panels are for the B6Su case in which the BH spin is aligned with orbital angular momentum. The observed differences are a consequence of how the debris responds to the orientation of the BH spin.

3.4. *Prompt and late accretion*

We observe an initial prompt phase of accretion when the star swings by the BH. This prompt accretion phase is followed by an intermediate phase in which material initially deflected by the BH slows down and begins to accrete. At late times, long after the end of our simulations, the characteristic $t^{-5/3}$ fallback behavior takes over.

Figure 7 shows the flow of matter through the IMBH's horizon during the first six seconds after the disruption takes place. The instant labeled t_{tidal} is the time at which the star enters the tidal radius. The horizontal dashed line labeled "noise" denotes the level of accretion due to the atmosphere used to model the vacuum regions. We observe that the magnitude of the prompt accretion rate decreases the more prograde an orbit is. Both B6S0 and B6Su disrupt at comparable distances from the central BH, but the peak accretion rate differs by almost two orders of magnitude.

As already pointed out in Section 3.3, the BH spin strongly affects what fraction of the star is accreted onto the BH soon (~ 2 s) after the star disrupts. Table 2 shows this accreted fraction for each case. In the B6Sd case, the star is completely accreted. On the other hand, the debris in the B6Su and B6Sa cases escapes almost in its entirety during the flyby. Notice also from Table 2 that the prompt accretion is also correlated with the maximum density ρ_{max} the WD is able to reach as a consequence of the tidal compression.

The late-time behavior consists of material raining back

onto the BH with a characteristic rate of accretion $\dot{M} \propto t^{-5/3}$ (Rees 1988; Phinney 1989). This rate is maintained as long as $dM/d\varepsilon_{kin}$, with ε_{kin} being the specific kinetic energy, is approximately constant (Lodato et al. 2009). We follow Rosswog et al. (2009) and compute the fallback time for each fluid element at a time long after disruption, based on data available at the end of the simulation. At this time, hydrodynamical interactions between the fluid elements are small, and each fluid element moves on an almost geodesic orbit. Figure 8 shows the results of these calculations. Clearly we recover the expected $t^{-5/3}$ behavior for return times longer than $t \gtrsim 200$ s. Notice that earliest times in Figure 8 are comparable to the late time accretion rates found during the simulation in Figure 7.

4. ELECTROMAGNETIC SIGNATURES

Ultra-close (i.e. $R_p \sim$ few R_g) tidal disruptions are violent events. The conversion of even a small fraction of gravitational energy into light would result in a powerful electromagnetic signature. In this section we will use the hydrodynamics results from our simulations to make order of magnitude estimates of the tidal disruption flare's luminosity, its characteristic photon energy, and the fallback material's electromagnetic signature as it eventually forms a slim accretion disk near the BH.

When the WD descends into the potential well of the BH, with the typical dynamical timescale of ~ 1 s, it acquires energy in excess of $\sim 10^{53}$ erg. Even if a tiny fraction of this energy gets converted into radiation on this dynamical timescale, it would lead to a huge luminosity which would be noticeable at cosmological distances. Furthermore, since the WD undergoes a substantial acceleration in the deep gravitational potential of the BH, the streams of matter from the disruption will approach speeds $V_p \simeq (GM_h/R_p)^{1/2} \simeq c(\beta R_g/R_t)^{1/2} \simeq 0.4\beta_6 c$, comparable to the speed of light. The streams of tidal debris later collide and transform a portion of their kinetic energy into thermal energy. Being heated by this process in excess of 10^9 K, the dense hot plasma quickly produces photons (Krolik & Piran 2011). These photons, however, are effectively trapped by the debris, capping the luminosity around the Eddington luminosity (Eddington 1926)

$$L_{Edd} = \frac{4\pi c\, G M_h m_p}{\sigma_T} = 1.4 \times 10^{41} \left(\frac{M_h}{10^3 M_\odot}\right) \text{erg s}^{-1}, \quad (16)$$

where m_p is the proton mass and σ_T is the Thomson cross-section. Notice that the equilibrium between the gravitational and spherical radiation fields is reached at a luminosity $L = 2L_{Edd} = 2.8 \times 10^{41}$ erg s^{-1} due to composition effects. The system can by far exceed L_{Edd} in the presence of a collimated outflow, especially in the first several minutes after the disruption. We elaborate on this tidal disruption phenomenon in a subsequent paper (Shcherbakov et al. 2012, in prep). In the present manuscript we limit ourselves to electromagnetic signatures at late times of months to years.

When the accretion rate falls below the Eddington rate $\dot{M}_{Edd}$, the accretion becomes radiatively efficient, radiating mostly in X-rays with luminosity $\sim L_{Edd}$. Assuming an efficiency of $\epsilon = 0.1$, this luminosity translates into an accretion rate

$$\dot{M}_{Edd} = \frac{L_{Edd}}{0.1 c^2} = 2.3 \times 10^{-5} \left(\frac{M_h}{10^3 M_\odot}\right) M_\odot \, yr^{-1}. \quad (17)$$
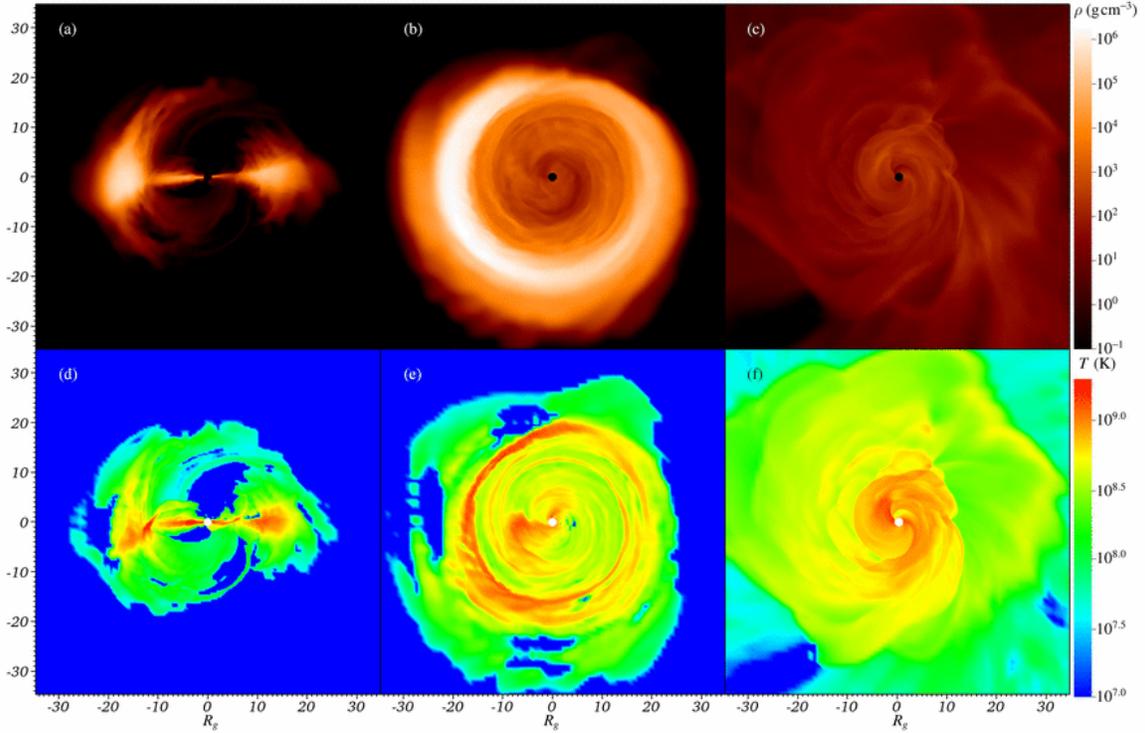
FIG. 6.— Snapshots in the orbital plane of the density (top row, in $g\,cm^{-3}$) and temperature (bottom row, in K) for runs B6Si and B6Su. The snapshots in the left column are for the case B6Si ~ 0.5 seconds after disruption. The middle and right columns correspond to case B6Su ~ 0.5 seconds and ~ 5.9 seconds after disruption, respectively.
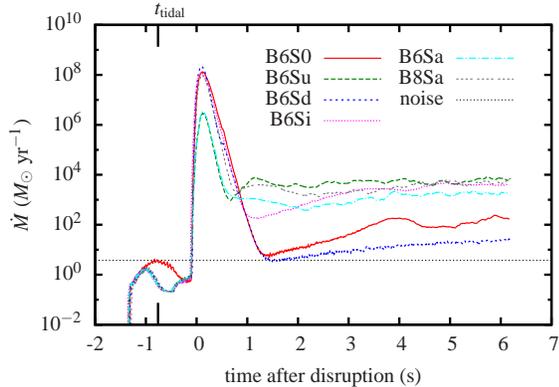
FIG. 7.— Accretion rate during the simulation. t_{tidal} indicates the approximate time when the WD enters within the tidal radius R_t. The horizontal dotted black line indicates the mass accretion which we observe initially around the black hole. It is a purely numerical artifact from the atmosphere used to model the vacuum regions.

FIG. 8.— Mass accretion rates computed from the estimated fallback times of the fluid elements. The solid line represents the $t^{-5/3}$ falloff predicted in Rees (1988); Phinney (1989).

4.1. Slim Disk Model

For our study we employ a slim disk model, developed and summarized in Abramowicz et al. (1988); Lasota (1994); Kawaguchi (2003); Sadowski (2009), of a simple one-zone vertically-integrated dynamical model. We compute modified black-body bremsstrahlung emission from the disk. For our radiation estimates, we assume that the angular momentum of the marginally bound debris accreting at late times, and thus the angular momentum of the disk, are aligned with the orbital angular momentum of the incoming WD. The disk model will then, in principle, be misaligned with the spin of the BH. We presume that, despite the misalignment, the slim disk extends down to ISCO radius computed for the aligned case. In our situation it is challenging to find a more reasonable set of assumptions for a geometrically thick slim disk. The ultimate answers require performing full numerical relativity simula-

The time elapsed until the accretion rate drops to $\dot{M}_{Edd}$ can be estimated based on the fallback times reported in § 3. We have demonstrated that the famous $t^{-5/3}$ fallback law (Rees 1988) is also present in our ultra-close encounters. From Figure 8, we observe that the accretion rate in all but the B6Sd case drops below $\dot{M}_{Edd}$ at times of $t_{Edd} \sim 1 - 2$ yrs. Thus the tidal events we are considering can, in principle, shine at Eddington luminosities for many years. The actual luminosity could be substantially sub-Eddington, though, if outflowing debris produced while the BH swallows matter at super-Eddington rates obscures the accretion flow. In this section we will first estimate the disk emission within a slim disk model and then consider the added effects of obscuration by the outflowing debris.

tions of the fallback regime, a task requiring modeling dynamical timescales 10^6 times longer than those addressed in the present study.

We take our heavy white dwarf to consist of approximately 50% carbon and 50% oxygen as suggested by stellar evolution computations by Mazzitelli & Dantona (1986). The same heavy white dwarf composition was assumed by both Rosswog et al. (2009) and Krolik & Piran (2011). Thus there is $1/14$ nuclei and $1/2$ electrons per one nucleon with mass $\simeq m_p$. In terms of nucleon density, the ion and electron densities are

$$n_{\text{ion}} = \frac{1}{14} n_{\text{nuc}} \quad \text{and} \quad n_e = \frac{1}{2} n_{\text{nuc}}, \quad (18)$$

respectively. The corresponding non-relativistic heat capacity of neutral and fully-ionized gas per single nucleon of temperature T are

$$c_{\text{neutral}} = \frac{3}{28} k_B T \quad \text{and} \quad c_{\text{ion}} = \frac{6}{7} k_B T, \quad (19)$$

respectively. The energy of full ionization is $E_{CNO} = \langle Z^2 \rangle 13.6\,eV = 680\,eV$ for the assumed composition, where $Z \approx 7$ is the charge of the nucleus. A CNO WD is thus fully ionized at $T > T_{\text{ion}} \sim 5 \times 10^6$ K. The molecular mass of the fully-ionized plasma is $\mu = 1.75$, and its density is $\rho = m_p n_{\text{nuc}}$.

A fully self-consistent model of a slim disk requires an estimate of the disk scale-height H. For a disk in the super-Eddington regime, $H/r = 1$ (Abramowicz et al. 1988; Kawaguchi 2003; Strubbe & Quataert 2009). In our simulations, circularization of debris happens within a distance $30R_g$ from the BH. We therefore consider a truncated disk located between the ISCO radius r_{ISCO} and the maximum radius $r_{\text{max}} = 30R_g$. The viscosity parameter is taken to be $\alpha = 0.1$. We solve the equations for the central temperature as detailed below, taking into account the effects of viscous heating, emission, and the finite heat capacity of matter. For simplicity, we follow Shakura & Sunyaev (1973) and set the viscous stress at the ISCO to zero. The energy release per unit disk area is then

$$F_+ = \frac{3 r_g \dot{M} c^2}{8 \pi r^3} \left[1 - \left(\frac{r_{\text{ISCO}}}{r} \right)^{1/2} \right]. \quad (20)$$

The accretion rate is expressed as

$$\dot{M} = 4 \pi r H \rho_c v_r, \quad (21)$$

where ρ_c is the one-zone density and $v_r > 0$ is the inflow velocity.

We adopt a beta disk model where the viscous stress is given by $t_{r\phi} = \alpha p_g$ with p_g being the gas pressure (Sakimoto & Coroniti 1981). A beta disk model is one of three options. In the standard Shakura & Sunyaev (1973) model, $t_\phi \propto p_{\text{tot}} = p_g + p_{\text{rad}}$, whereas in the "mean field" models $t_\phi \propto \sqrt{p_g p_{\text{tot}}}$ (see e.g. Done & Davis 2008 for a review). There is no definitive answer yet about which model better describes stress in a radiation-dominated accretion disk. The beta disk model $t_{r\phi} = \alpha p_g$ assumption leads to a radial velocity of plasma

$$v_r \approx \alpha c_s = \alpha \sqrt{\frac{k_B T_c}{\mu m_p}}, \quad (22)$$

where c_s is the isothermal sound velocity. The expression (22) for radial velocity, though not fully self-consistent, helps to avoid the infinite increase of the density near the ISCO inherent to early slim disk models (Abramowicz et al. 1988).

The accretion disk emits predominantly bremsstrahlung radiation. Since the scattering cross-section in the disk is much higher than the absorption cross-section, the emission spectrum is described by a modified black body spectrum (Rybicki & Lightman 1979; Czerny & Elvis 1987; Kawaguchi 2003). The photon production rate via bremsstrahlung is (Rybicki & Lightman 1979; Katz et al. 2010)

$$Q = \sqrt{\frac{8}{\pi}} \alpha_f Z^2 n_{\text{ion}} n_e \sigma_T c \sqrt{\frac{m_e c^2}{k_B T_e}} \Lambda_{\text{eff}} g_{\text{eff}} \, \text{cm}^{-3} \text{s}^{-1}, \quad (23)$$

where $\Lambda_{\text{eff}} \sim g_{\text{eff}} \sim 1$, $\alpha_f \approx 0.00729$ is the fine structure constant and σ_T is the Thomson cross-section. With the high densities, the production rate Q is high so the radiation quickly dominates internal energy and pressure.

Let us estimate the equilibrium temperature of this radiation-dominated flow. The typical nucleon density in the simulation varies from $n_{\text{nuc}} \sim 10^{25}\,\text{cm}^{-3}$ near the BH, to a minimum of $n_{\text{min,nuc}} \sim 8 \times 10^{20}\,\text{cm}^{-3}$. The typical virial temperature is $T_{\text{ion}} \sim 10^{11}$ K. As photons are produced, the equilibrium implies

$$\frac{6}{7} n_{\text{nuc}} k_B T_{\text{ion}} = a_{BB} T_{\text{ph}}^4, \quad (24)$$

leading to photon temperatures $T_{\text{ph}} \sim 3 \times 10^8$ K. The timescale for reaching equilibrium can be estimated as

$$t_{eq} \sim \frac{a_{BB} T_{\text{ph}}^4}{k_B T_{\text{ph}}} \frac{1}{Q(T_{\text{ph}})} = 9 \times 10^{10} \frac{T_{\text{ion}}^{7/8}}{n_{\text{nuc}}^{9/8}} \sim 10^{-8} \text{s}, \quad (25)$$

which is significantly shorter than the dynamical timescale $t_{\text{orb}} \sim 1$ s.

We work in the diffusion approximation of high optical depth to find the surface temperature. The corresponding scattering opacity, $\tau_{\text{sc}} \gg 1$, is much larger than the bremsstrahlung absorption opacity τ_{abs}. The electron scattering opacity is

$$\kappa_{\text{sc}} = \frac{\sigma_T n_e}{m_p n_{\text{nuc}}} \approx 0.2 \text{cm}^2 \text{ g}^{-1}, \quad (26)$$

whereas the absorption opacity is

$$\kappa_{\text{abs}} = \frac{(1 - e^{-x}) e^6 h^2 Z \rho_c}{3 c k_B^3 m_e m_p^2 T_s^{7/2} x^3} \sqrt{\frac{2\pi}{k_B m_e}}$$

$$= \frac{4.4 \times 10^{25} (1 - e^{-x}) \rho_c}{T_s^{7/2} x^3} \quad (27)$$

where $x = h\nu / (k_B T)$ (Shapiro & Teukolsky 1986). The total emitted power through one side of the disk with surface temperature T_s is then

$$F_- = \frac{a_{BB} c}{4} T_s^4 \sqrt{\frac{\bar{\kappa}_{\text{abs}}}{\bar{\kappa}_{\text{sc}}}}, \quad (28)$$

where, in a one-zone model, the central density is taken as a proxy for the surface density. Here $\bar{\kappa}$ denotes mean opacities. We use here the Rosseland mean opacity (Shapiro & Teukolsky 1986), $\bar{\kappa}_{\text{abs}} = 3.2 \times 10^{22} Z \rho_c T_s^{-7/2}$.

The energy flux delivered to the surface is

$$F_{\text{surf}} = F_- = \frac{a_{BB} c}{3} \frac{T_c^4}{\tau_{\text{sc}}}. \quad (29)$$

To sustain the radiation flow through the surface, this energy flux is equal to the radiated flux. Thus from (28) and (29) we obtain that $T_s \propto T_c^{16/9}$. In a slim disk, cooling does not balance heating, $F_+ \neq F_-$. The residual energy is stored within the accreting material. The energy balance can then be written as

$$Q = F_+ - F_-, \quad (30)$$

where the residual energy per unit surface area is given as

$$Q = \Delta U + A = \frac{4}{3} H a_{BB} T_c^4 \left(3 \frac{1}{T_c} \frac{dT_c}{dt} - \frac{1}{\rho_c} \frac{d\rho_c}{dt} \right), \quad (31)$$

where $dt = -dr/v_r$. We solve the equations (21) and (22) for the central density ρ_c. The central temperature T_c is obtained from equation 30 with the help of (20), (29) and (31). Given the central density and temperature, we calculate the surface temperature T_s from (28) and (29) as well as the corresponding spectrum.

Figure 9 shows the dependence of surface temperature T_s on radius R for the accretion rates inferred from the output of the B6Su simulation. Later times correspond to lower accretion rates. The temperature T_s is, in general, higher at higher accretion rates, i.e. earlier times. This is because the energy release per unit time goes up with accretion rate while the radiating surface area stays constant. At very low $\dot{M}$, our slim disk accretion model resembles the standard thin disk model (Shakura & Sunyaev 1973) so $T_s \rightarrow 0$ at the ISCO. In contrast, T_s at the ISCO saturates at the highest accretion rates. With little energy release, $F_+ \gg F_-$, the energy density is proportional to the accretion rate $Q = F_+ \propto \dot{M}$. In turn, the scattering opacity is also proportional to the accretion rate $\tau_{sc} \propto n_e \propto \dot{M}$. The energy density of radiation is proportional to T_c^4. In addition there is a factor of $\dot{M}$ in both the numerator and the denominator of the expression (29) for the surface flux. In the end, $F_{surf} \propto \dot{M}$ in the radiatively inefficient regime.
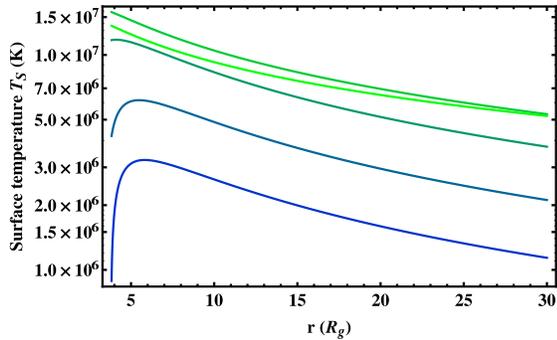
FIG. 9.— Surface temperature of the slim disk for the case B6Su at various times after the disruption. From top to bottom: at $t = 8$ months, $t = 2$ months, $t = 3$ years, $t = 10$ years, and $t = 30$ years, respectively. As time progresses the accretion rate decreases from $\dot{M} \sim 4000 \dot{M}_{Edd}$ to $\dot{M} \sim 4 \dot{M}_{Edd}$. The inner disk boundary is chosen to be at $r_{ISCO} = 3.83\, R_g$.

The corresponding disk spectra are shown in Figure 10. From top to bottom, νL_ν as a function of energy are shown at 2, 8 months, then 3, 10 and 30 years, respectively. Like T_s, the hard tail of the spectrum also saturates at the highest accretion rates. On the other hand, the low-energy tail does not saturate at $\dot{M} \sim 4000 \dot{M}_{Edd}$. This is because the radiation time is still shorter then or comparable to the advection timescale at large distances from the BH, where the low-energy tail is

emitted. As the accretion rate drops with time, the luminosity (the area under the curve) also drops.
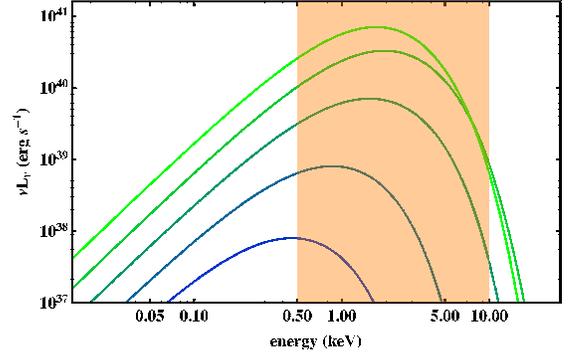
FIG. 10.— Spectrum for the slim disk formed following the tidal disruption at various times. The spectra shown corresponds to the case B6Su as in Figure 9. From top to bottom: at $t = 2$ months, $t = 8$ months, $t = 3$ years, $t = 10$ years, and $t = 30$ years, respectively. The inner boundary is chosen to be at $r_{ISCO} = 3.83R_g$. The spectrum gets harder with time, but the luminosity decreases.

The integrated luminosity is shown in Figure 11 for the case B6Su. At late times, i.e. $t \gtrsim 2$ years, the luminosity is proportional to the accretion rate and decreases as $t^{-5/3}$. Specifically, we estimate a luminosity $L \simeq 0.05 \dot{M} c^2$ for our disk model. Notice that the estimated luminosity in a fully general relativistic model is $L \simeq 0.091 \dot{M} c^2$ for a thin disk without radiative transfer effects (Bardeen et al. 1972). At early times $t \lesssim 2$ years the luminosity saturates at about the Eddington value $L_{Edd} = 1.4 \times 10^{41} \text{erg s}^{-1}$. The luminosity at times $t < 2$ months is not reliable, since the slim disk model may not be an adequate representation of accretion at rates $\dot{M} > 4000 \dot{M}_{Edd}$. For instance, when the outflow from the inner disk is present, the luminosity may further increase (Owocki & Gayley 1997; Shaviv 2001; Begelman 2001; Dotan & Shaviv 2011). Such a computation is, however, beyond the scope of the paper.
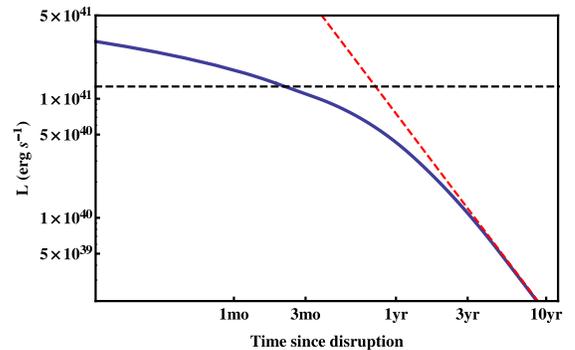
FIG. 11.— Light curve (solid line) of the slim disk following the tidal disruption in the case B6Su. The inner boundary is chosen to be at $r_{ISCO} = 3.83R_g$. The luminosity decreases with time, first slowly, then sharply below Eddington (horizontal dashed line). The behavior asymptotes to a power-law $L = 0.05\dot{M}c^2 \propto t^{-5/3}$ at low luminosity (inclined dashed line), when all thermal energy is radiated on the way to ISCO. The model cannot be trusted if luminosity significantly exceeds Eddington value.

We consider now the radiative properties of disks from the other cases with different penetration parameters β, spins magnitudes $a^\star$, and spin orientations. Figure 12 shows the disk spectra at $t = 1$ yr after the disruption for all the cases

studied. In all cases, we assumed a slim disk with inner boundary at r_{ISCO} and outer boundary at $30 R_g$.

The spectra in Figure 12 are different because of two factors. The first contributing factor is the accretion rate $\dot{M}$, which we parameterize by the fallback time. More debris falls back onto the BH in the B6Sa case than in the other cases (see Figure 8). Therefore the spectrum for the B6Sa case is systematically brighter. Similarly, the lower accretion rate for the B6Si case makes its spectrum systematically weaker than the others. We found that one can achieve coincidence of spectra among all $a^\star = 0.6$ cases with a time shift. That is, at times when the accretion rates $\dot{M}$ are identical for different simulations, the spectra are also identical. The spectrum for the B6Sa case at about $t = 16$ months is identical to the spectrum for the B6Su case at $t = 12$ months and to the spectrum from the B6Si case at about $t = 9$ months. Also, more matter is swallowed by the BH initially in the B8Sa case when compared with the B6Sa case, but at later times, less matter that will be eventually accreted is scattered. Thus the fall back time is lower for the B8Sa case, resulting in a less luminous spectrum. The spectra also vary because of changes in the ISCO radius. For instance, the ISCO is further from the BH in the B6S0 case with spin $a^\star = 0$. Since little energy release is taking place inside $r_{ISCO} = 6 R_g$, its spectrum is significantly softer.

4.2. Obscuration

The edge-on view of a slim disk is self-obscured. The spectrum of a self-obscured disk is not easy to determine. We can approximate the spectrum by assuming that the thick outer edge at $r = 30 R_g$ emits modified black body radiation the way the top of the slim disk does. The corresponding edge-on spectrum is included in Figure 12 as the black dotted line. It is softer, since only the material far from the BH contributes. The surface area of the thick outer edge is large, though, resulting in a raised low-energy tail.
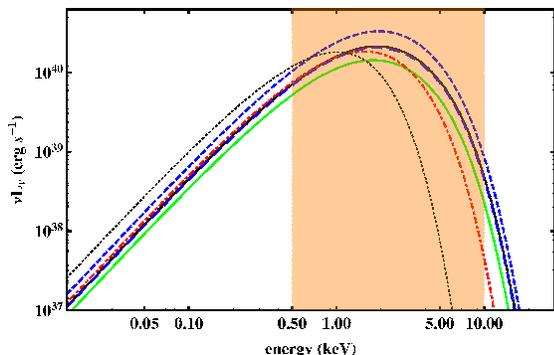
FIG. 12.— Spectra of our slim disk models at $t = 1$ yr: B6Su case (top solid/black), B6Si case (bottom solid/green), B6Sa case (short-dashed/blue), B8Sa case (long-dashed/blue), B6S0 case (dot-dashed/red). Differences are due to changing spin and fallback time. Dotted line corresponds to an edge-on view of a slim disk for b6ap6 simulation. The edge-on disk has a softer spectrum and a comparable luminosity.

Besides exploring the properties of a slim disk, we investigated whether the emission from the disk is visible through the outflowing debris surrounding the disk. Figure 13 shows the $(\cos\theta, \phi)$ directions in which the debris is scattered in the "sky" from the BH point of view. We considered only the material outside a sphere of radius $150 R_g$, corresponding to the boundary between the bound and the unbound matter at

time $t \approx 6$ s after the disruption. The unbound matter travels essentially along straight lines at $t \approx 6$ s so Figure 13 adequately represents the angular distribution of matter at late times. White color in Figure 13 indicates there is no matter traveling in that direction whereas all darker colors indicate the presence of gas.

The optical depth is very high at directions that are not denoted by white. The inner disk would be completely obscured along those directions. The left panel in Figure 13 shows the distribution of the scattered debris for the B6Si case. Notice that although the debris is scattered all over the sky, there are some preferential directions manifest as a sinusoid in the $(\cos\theta, \phi)$ plane. On the other hand, in the case B6Su shown on the right panel, the debris is scattered preferentially in the disruption plane. Thus the orientation of BH spin determines the direction of debris outflow for ultra-close encounters.

We consider now the situation in which we view a WD-BH system with an unknown orientation. Recall that we have assumed that the disk at late times is fully aligned with the initial disruption plane. As discussed before, the disk can, in principle, be viewed both edge-on or face-on, although the edge-on disk is self-obscured and has a peculiar spectrum (see Figure 12). The probability the disk is obscured by the outflowing debris is proportional to the solid angle subtended by the debris. This solid angle corresponds to the normalized surface area on the $(\cos\theta, \phi)$ plane (see Figure 13). There may in principle be four different types of obscuration: i) edge-on self-obscured disk also obscured by outflowing debris, ii) edge-on self-obscured disk unobscured by outflowing debris, iii) face-on disk obscured by outflowing debris, and iv) face-on completely unobscured disk.

When the height of the photosphere equals the disk height $H = r$ (inclination $\theta = 45°$), the probability to encounter a self-obscured edge-on disk is $p_{edge} = 71\%$. The obscuration probability by outflowing debris is depicted in Figure 14 for both edge-on and face-on disks. The panels show the probability as a function of debris location at $t = 6$ s after the disruption. At that time, the boundary between the bound and the unbound matter is located at $150 R_g$. Thus, this obscuration probability is also the obscuration probability p_{obs} for days to years later. The obscuration probability $p_{obs|edge}$ of an edge-on disk can be inferred from the left panel. Since most debris is scattered in the disruption plane, this probability is relatively high. The values reach $p_{obs|edge} \approx 50\%$, practically independent of spin value, spin orientation or penetration factor. The obscuration probability of a face-on disk $p_{obs|face}$ can be inferred from the right panel. Only the fully misaligned case B6Si scatters significant amount of debris perpendicular to the disruption plane, which leads to relatively high $p_{obs|face} \approx 40\%$ for this simulation. Partially and fully aligned simulations all scatter matter within $45°$ from the disruption plane, and thus cannot obscure the face-on disk, so that $p_{obs|face} = 0\%$. The total obscuration probability is

$$p_{obs} = p_{obs|face}\, p_{face} + p_{obs|edge}(1 - p_{face}). \qquad (32)$$

The values are $p_{obs} \approx 50\%$ for the B6Si case and $p_{obs} \approx 30\%$ for the B6Su, B6Sa, B8Sa and B6S0 cases. The misaligned simulation with $\beta = 8$ yields a marginally higher $p_{obs|edge} = 52\%$ compared to a similar simulation with $\beta = 6$ for which $p_{obs|edge} = 44\%$. As expected, deeper penetration results in wider scattering of debris. However, surprisingly, partially aligned and fully aligned simulations with $\beta = 6$ and $a^\star = 0.6$ yield almost the same obscuration probabilities.

We have previously stated that if there is debris along the
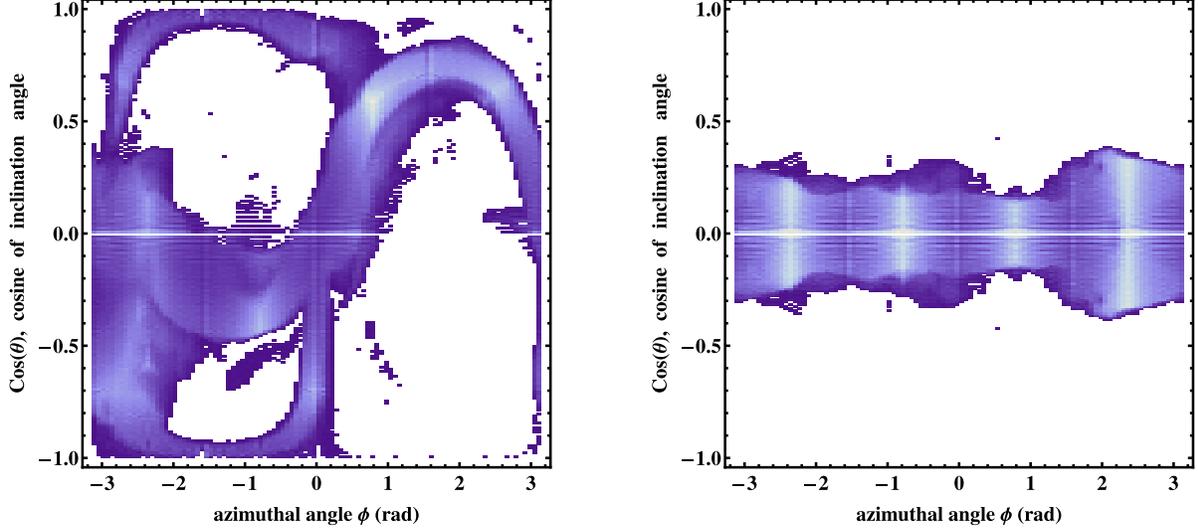
FIG. 13.— Obscuring gas beyond $r = 150 R_{\rm g}$ on the $(\cos\theta, \phi)$ plane for the fully misaligned spin case B6Si (*left* panel) and fully aligned spin case B6Su (*right* panel). Here θ is an inclination angle of the disruption plane and ϕ is the azimuthal angle with respect to the BH's point of view (See Fig. 2). *Left:* The gas in this case is scattered to all angles, yet there are substantial holes through which the inner disk could be visible. *Right:* For this case, the disk will be visible in directions away from the disruption plane.
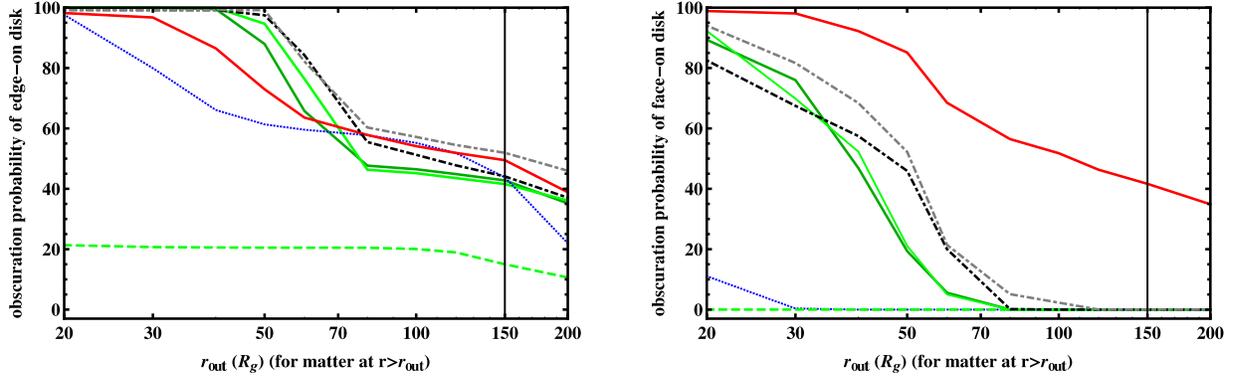
FIG. 14.— Obscuration by debris as a function of the debris beyond a radius $r_{\rm out}$ from the BH. The obscuration probability is the probability that the inner disk is not seen from a random viewing angle. *Left:* obscuration probability for an edge-on disk with inclination angles above $45°$ (assuming aligned disk). *Right:* obscuration probability for a face-on disk with inclination angles below $45°$. The boundary of bound/unbound matter is around $r = 150 R_{\rm g}$ at $t = 6$ s after disruption. The unbound matter moves approximately radially so the probabilities at $r_{\rm out} = 150 R_{\rm g}$ (denoted by a vertical line) correspond to obscuration probabilities days to years later. Lines types correspond to case B6Si (upper solid red), B6Su (two lower solid green lines: the darker ones are computed at earlier time $t = 5.4$ s), B6S0 (blue dotted), B6Sd (green dashed), B6Sa (dark dot-dashed), and B8Sa (light dot-dashed). The obscuration probability of an edge-on disk is about $\approx 50\%$ regardless of spin alignment. Only the B6Sd case, with very little debris, exhibits little edge-on obscuration. In turn, the obscuration probability of a face-on disk depends on alignment. The fully misaligned B6Si case is obscured at 50% for nearly face-on disk orientations whereas the partially misaligned and aligned cases exhibit no obscuration of a face-on disk.

line of sight, then the inner disk is obscured. However, the optical depth of debris decays as the debris expands and eventually becomes transparent. Let us estimate the time $t_{\rm trans}$ when the optical depth of X-ray absorption equals unity $\tau_{\rm abs} = 1$. The actual time will of course depend on the line of sight. The debris consists mostly of neutral carbon and oxygen with high absorption cross-section $\sigma_{\rm abs} \simeq 2 \times 10^{-20} {\rm cm}^{-2}$ within $0.5 - 10$ keV photon energy range (Henke et al. 1993). The typical outflow velocity of the debris is a substantial fraction of the speed of light $v_{\rm out} \approx 0.15 c$. The transparency time is then

$$t_{\rm trans} = \sqrt{\frac{f_{\rm unb} M_{\rm wd} \sigma_{\rm abs}}{56\pi m_p p_{\rm obs} v_{\rm out}^2}} \qquad (33)$$

where $f_{\rm unb}$ is the fraction of outbound material. From our simulations, we found that $f_{\rm unb} \simeq 22\%$ ($f_{\rm unb} \simeq 60\%$) for the

B6Si (B6Su) case. With our obscuration probability estimate $p_{\rm obs} \simeq 50\%$ ($p_{\rm obs} \simeq 30\%$) for the B6Si (B6Su) case, we find that $t_{\rm trans} \approx 2$ yr ($t_{\rm trans} \approx 4$ yr). The transparency time given by equation (33) is an underestimate, since marginally unbound matter moves at speeds lower than the average $v_{\rm out}$.

5. GRAVITATIONAL WAVE EMISSION

In addition to producing the electromagnetic signatures discussed in previous sections, tidal disruptions events are potential sources of GW radiation. A disruption event generates a burst of GWs lasting $t \sim R_{\rm p}/V_{\rm p} \sim (R_{\rm p}^3/GM_{\rm bh})^{1/2}$ (Kobayashi et al. 2004; Rosswog et al. 2009). The GW burst produced will have a characteristic frequency $f \sim (GM_{\rm bh}/R_{\rm p}^3)^{1/2}$ and amplitude $h \sim (GM_{\rm wd}R_{\rm g})/(c^2 R_{\rm p} D)$, with D the distance to the BH. For the case of a WD disrupted

by an IMBH (Rosswog et al. 2009),

$$f \sim 0.78 \, \beta^{3/2} \left(\frac{R_{\mathrm{wd}}}{0.86 R_\oplus} \right)^{-3/2} \left(\frac{M_{\mathrm{wd}}}{1 M_\odot} \right)^{1/2} \mathrm{Hz} \qquad (34)$$

$$h \sim 5.9 \times 10^{-20} \beta \left(\frac{D}{20 \, \mathrm{kpc}} \right)^{-1} \left(\frac{M_{\mathrm{wd}}}{1 M_\odot} \right)^{4/3}$$

$$\left(\frac{R_{\mathrm{wd}}}{0.86 R_\oplus} \right)^{-1} \left(\frac{M_{\mathrm{BH}}}{10^3 M_\odot} \right)^{2/3}. \qquad (35)$$

These estimates place the GWs from these events at the low frequency edge of the advanced LIGO design sensitivity range. At this edge, the equivalent strain noise is $\sim 10^{-22} \, \mathrm{Hz}^{-1/2}$ (LIGO Scientific Collaboration 2009).
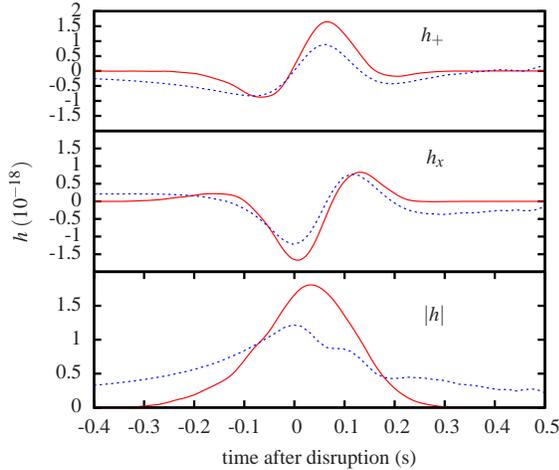
FIG. 15.— Gravitational wave strain as calculated in full general relativity (solid red) and from applying the quadrupole formula (dashed blue) for B6Sa at a distance of 20 kpc. Depicted are the two polarizations, h_+ (top) and $h_\times$ (middle), as well as the amplitude (bottom).

In Figure 15, we compare the GW strain extracted from the spacetime (solid red) to that obtained using the quadrupole formula Rosswog et al. (2009) applied to the WD's center of mass trajectory (dashed blue) for B6Sa. While the qualitative behavior of the two polarizations, h_+ (top) and h_x (middle), are similar, the fully nonlinear GW strain differs in both amplitude and phase.
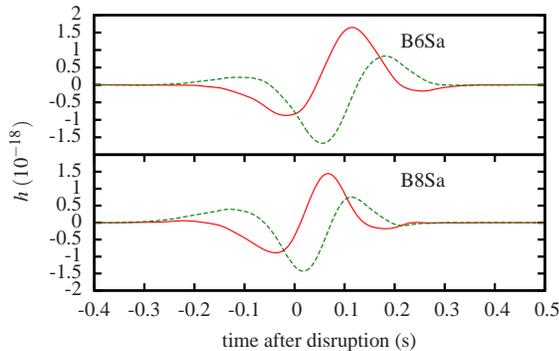
FIG. 16.— Gravitational wave strain h from disruption events at a distance of 20 kpc. Depicted are the two polarizations, h_+ (solid red line) and $h_\times$ (dashed green line) for cases B6Sa (top) and B8Sa (bottom).

In Figure 16, we show the GW strain as a function of time for disruption events at a distance of 20 kpc. Depicted are
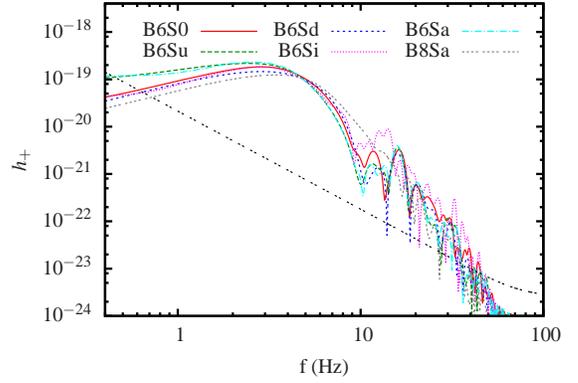
FIG. 17.— Power spectrum of the h_+ polarization of GWs for all considered cases. We include the advanced LIGO design sensitivity (double-dashed line) for comparison. All cases indicate a characteristic frequency of 3.2 Hz. At low frequencies, ~ 1 Hz, there is a hint of a dependence of the amplitude on the spin orientation.

the two polarizations of GWs: h_+ (solid red line) and $h_\times$ (dashed green line) for cases B6Sa (top) and B8Sa (bottom). Time $t = 0$ denotes approximately the time when the disruption takes place. Evident is the burst-like nature of the GWs. Notice that both cases exhibit comparable burst duration and strain amplitude. This is expected since the only difference between B6Sa and B8Sa is their value of β. Although we have stated that case B6Sa has $\beta = 6$ and B8Sa a $\beta = 8$, from Table 2, we have that the actual penetration factor for both cases is $\beta^* \simeq 10$. Interestingly, the other cases also showed comparable burst durations, ~ 4s, suggesting a weak dependence with the orientation of the spin and penetration factor.

Figure 17 shows the power spectrum for all the cases investigated where we assume that the events took place at a distance of 20 kpc. All cases indicate a characteristic frequency of ~ 3.2 Hz. This is about an order of magnitude smaller that the estimated frequency using (34) with $\beta^* \simeq 9$, the average real penetration factor (see Table 2). This should not be too surprising since rough estimates using (34) and (35) do not take into account, among other things, spin effects. Similarly, Figure 17 shows characteristic strain amplitudes of $\sim 10^{-18}$, an order of magnitude higher than the estimate using (35) with $\beta^* \simeq 9$.

At low frequencies, ~ 1 Hz, we note that the B6Sa and B6Su cases in particular have higher strain amplitude than the rest. Interestingly, these are the same cases which, as seen in Fig. 7, exhibit significantly lower prompt accretion in the first second after disruption and higher accretion in the $\sim 1-2$ s after disruption. The third case with higher prompt accretion in the $\sim 1-2$ s interval, B8Sa, however, exhibits the lowest low-frequency tail. This suggests that relativistic effects create an entangled parameter space involving spin and penetration factor during the disruption phase. Given that the actual penetration factors in all the cases were comparable, $7.6 \leq \beta^* \leq 11$, further study is required to explore this parameter space.

Synergistic observations of electromagnetic emission from the prompt accretion discussed in Section 4, together with GW detections, may provide ways to measuring the spin of the BH since in both instances the emission seems to depend, although not strongly, on the spin orientation. We are currently expanding the parameter space covered by our simulations to investigate this dependence in more detail. Multi-messenger observations will be, of course, only possible if the prompt electromagnetic emission is not obscured by the debris surrounding the BH. If such obscuration prevents ob-

serving prompt accretion, the detection of a GW burst would, in that case, still serve as an identifying precursor to the observations of the late fallback electromagnetic emission.

6. RATES AND OBSERVATIONAL PROSPECTS

6.1. *Tidal Disruption Rates*

The disruptions of stars by BHs are rare events. More studied are tidal disruptions of stars by SMBHs in galactic centers. Their rate $10^{-5}\mathrm{yr}^{-1}$ per galaxy was predicted theoretically by (Magorrian & Tremaine 1999; Wang & Merritt 2004) and found consistent with observations by ROSAT (Donley et al. 2002), XMM-Newton (Esquej et al. 2007), and GALEX (Gezari 2010). The volume density of SMBHs is about (Tundo et al. 2007)

$$n_{SMBH} = 10^{-2}\mathrm{Mpc}^{-3}, \qquad (36)$$

which leads to tidal disruption rate per unit volume

$$R_{SMBH} = 10^2\mathrm{yr}^{-1}\mathrm{Gpc}^{-3}. \qquad (37)$$

The rate of disruption of stars in globular cluster (GC) is much less certain. Baumgardt et al. (2004) predicts that, for a GC with $10^3 M_\odot$ BH, the optimistic disruption rate of stars is $10^{-7}\mathrm{yr}^{-1}$ per GC. According to McLaughlin (1999), the mean GC mass is $M_{GC} = 2.4 \cdot 10^5 M_\odot$, which is larger than clusters considered in Baumgardt et al. (2004). For a largest cluster simulated by Baumgardt et al. (2004) with $N = 131,072$ stars they find 15% of disrupted stars to be WDs. Therefore the optimistic rate of WD-IMBH tidal disruptions is

$$D = 1.5 \cdot 10^{-8}\mathrm{yr}^{-1} \qquad (38)$$

per cluster. The number of GCs changes dramatically from one galaxy to another (Harris 1991). However, GCs have about constant formation efficiency $\epsilon_{cl} = 0.0026$ (McLaughlin 1999), which is the ratio of GC mass to the initial mass of gas in a galaxy. We assume half of baryonic matter in galaxies, take the Hubble constant $H_0 = 70.4\mathrm{km\ s}^{-1}\mathrm{Mpc}^{-1}$ and current baryonic content $\Omega_b = 0.00456$ (Komatsu et al. 2011) and find the number density of GCs as

$$n_{GC} = 0.5\frac{3H_0^2}{8\pi G}\frac{\Omega_b \epsilon_{cl}}{M_{GC}} = 34\mathrm{Mpc}^{-3}. \qquad (39)$$

This density overpredicts the number of GCs in the Milky Way, but is consistent with the overpopulated with GCs elliptical galaxies such as M87. It is not known, what percentage of GCs contains an IMBH. For an optimistic estimates, we take one $10^3 M_\odot$ IMBH per cluster. Then, the disruption rate per unit volume is

$$R_{WD-IMBH} = 500\mathrm{yr}^{-1}\mathrm{Gpc}^{-3}. \qquad (40)$$

This rate is even higher than R_{SMBH}, but the WD-IMBH disruptions are much less luminous, so they are harder to find. Also, the rates of tidal disruptions in GCs are quite uncertain (Baumgardt et al. 2004), so even disproving the rate given by equation (40) does not necessarily disprove the hypothesis that every GC has an IMBH.

Out of all tidal disruptions, we focused on ultra-close ones with the ratio of tidal radius to pericenter distance about $\beta = 6$. These constitute a fraction of all disruptions. For a realistic triaxial potential of a GC, chaotic feeding would prevail (Merritt & Poon 2004). Chaotic feeding leads to tidal disruption probability proportional to R_p for objects coming within

pericenter distance R_p, as a clear consequence of gravitational focusing. Therefore, tidal disruptions with $\beta > 5$ constitute $1/5$ of all events. The correspondent optimistic rate is

$$R_{WD-IMBH,\beta>5} = 100\mathrm{yr}^{-1}\mathrm{Gpc}^{-3}. \qquad (41)$$

6.2. *Observations of X-ray Flares*

Considered ultra-close tidal disruptions manifest with a year-long X-ray flare at an Eddington luminosity off the center of the galaxy. Tidal disruptions by SMBHs rather produce an optical flare (Strubbe & Quataert 2009) in the center of the galaxy. Let us explore if the optimistic high rates of tidal disruptions are consistent with past observations and if the future observations have a chance of catching such an event.

ROSAT survey probed all sky down to $F_{ROSAT} = 4 \cdot 10^{-13}\mathrm{erg\ s}^{-1}\mathrm{cm}^{-2}$ flux within $0.1-2.4$ keV band (Voges et al. 2000). The peak of X-ray tidal disruption spectrum at 1 yr (see Figure 12) is at about 2 keV, so that more than half of photons are captured. Taking luminosity $L = 4.3 \cdot 10^{40}\mathrm{erg\ s}^{-1}$ of B6Su simulation at $t = 1$ yr we obtain the maximum distance of

$$d_{ROSAT} = 25\mathrm{Mpc}. \qquad (42)$$

Therefore, the expected number of observed WD-IMBH disruptions is $N_{ROSAT} = 0.015$, which is consistent with no events. With Chandra, 100 photons can be obtained over 30 ks from the source 200 Mpc away and over 1 Ms from the source 1.2 Gpc away, according to the Portable, Interactive Multi-Mission Simulator (PIMMS; Mukai 1993). However, owing to a small field of view of the satellite, the careful choice of field is required to observe at least one event.

In turn, the future mission like Wide Field X-ray Telescope (WFXT) (Conconi et al. 2010) can detect a substantial number of events. It is much more sensitive than ROSAT and observes in the same waveband. The flux limits of $3 \cdot 10^{-17}$, $5 \cdot 10^{-16}$, and $3 \cdot 10^{-15}$ for deep, medium and wide surveys with correspondent solid angles 100, 3000, and 20,000 deg^2 yield maximum event distances 2.5 Gpc, 600 Mpc, and 245 Mpc. This translates into 76, 33, and 16 WD-IMBH disruptions or 5 times fewer ultra-close disruptions.

Tidal disruptions can also produce powerful prompt super-Eddington X-ray flare with the duration of minutes in addition to the Eddington-limited X-ray flux on the timescale of ~ 1 yr. The lightcurve, spectrum and detection prospects will be discussed in the next paper Shcherbakov et al., (2012, in prep.).

7. DISCUSSION AND CONCLUSIONS

Our work addresses disruptions of WDs by IMBHs. This is the first fully general-relativistic study that includes both strong gravity (the metric of the spinning BH) and dynamical gravity effects (GWs). We focused on ultra-close disruptions, where the periapsis radius is comparable to the BH gravitational radius. Our study presents for the first time results on the influence of the BH spin on the disruption.

Our study made some simplifying assumptions. Instead of employing a degenerate equation of state for the WD, we used an ideal gas law. This is, however, expected to have a very minor effect on dynamics. If the entropy is approximately constant, the evolution of a degeneracy pressure supported star is identical to that with an ideal gas pressure. The choice of pressure prescription does not matter until shocks and turbulence take over. Similarly, the absence of explicit radiation pressure does not influence the initial stages of the disruption. Cold outflowing debris may not have significant radiation pressure

support, and only the fallback disk will be radiation pressure dominated. Radiation emitted from the inner disk may halt the infall of the marginally bound debris. However, the disk is self-obscured near the disruption plane where most of debris is scattered, and the photon mean free path is quite small. The photons cannot thus effectively transfer energy from the inner flow to the outer flow to unbind the debris. Should radiation pressure be included, the same internal energy contribute a radiation pressure smaller than the gas pressure, and thus the total pressure in the medium would be lower.

Our study does not include nuclear reactions, believed to be important for deep WD disruptions (Rosswog et al. 2009). Temperature-density tracks of the matter in our simulations as depicted in Figure 4 are comparable to those found in Figure 14 of Rosswog et al. (2009). The tracks suggest that nuclear burning of carbon and oxygen should occur in the cases we studied. The additional energy gained in C and O burning into Fe is 1 MeV per nucleon (Dursi & Timmes 2006). This translates to a gain of energy of $\sim 0.001\,M\,c^2$. On the other hand, the descent into the gravitational potential of the BH yields energies of $\sim 0.1\,M\,c^2$ for a periapsis radius of $R_{\mathrm{p}} \sim 10\,R_{\mathrm{g}}$. The dispersion of debris energies after ultra-close disruptions is also large. Thus, the extra $0.001\,M\,c^2$ energy from the burning will not likely have a dramatic effect on the debris. The optical lightcurve may indeed change after an initially cold white dwarf is heated by nuclear reactions, but the influence on the fallback disk is expected to be small.

A realistic fallback disk simulation should incorporate magnetic fields. Magnetic fields give rise to large viscosity and allow the disk to self-consistently accrete. The assumed parameter α will be a proxy for viscosity until magnetized simulations can be run for a sufficiently long time. The presence of magnetic fields may readily lead to an outflow (Blandford & Payne 1982), which may boost luminosity far above the Eddington limit or radiation pressure itself may drive an outflow under certain circumstances (Shaviv 2001). The duration of our simulations (~ 7 s) was too limited to directly model the fallback. The temporal dependence of accretion rate depicted in Figure 8 is a ballistic guess, based on a confirmed flat distribution of mass over energy. Any outflow or halted inflow at late times may result in deviations of the fallback law from $\dot{M} \propto t^{-5/3}$.

We make a distinction in the paper between the face-on and edge-on disks. In reality, only minor differences between these orientations may exist. The disk with extreme accretion rate may drive a wind or have a corona, which might completely obscure the very inner portions of the disk. In such a case, the spectrum would be similar to an edge-on spectrum regardless of orientation. The precise quantitative predictions of spectra will only be possible with detailed numerical simulations of the fallback accretion.

Our study should be viewed as a step towards realistic tidal disruptions of WDs by IMBH. Some of the conclusions may hold up despite our limited understanding of matter fallback and super-Eddington accretion flows. Our main conclusions are:

- For a non-spinning BH and a BH with a spin aligned or misaligned with the orbital angular momentum, the debris after disruption forms a thick accretion disk.

- For misaligned spins, frame-dragging effects scatter the debris around the BH and will often obscure the inner region from observation.

- There is a qualitatively different behavior before and after a timescale of ~ 1 yr, when the accretion rate approaches Eddington accretion rate. The accretion flow luminosity stays around L_{Edd} before ~ 1 yr and starts dropping as $t^{-5/3}$ afterwards.

- The spectrum peaks at soft X-rays. The spectra are similar to thin disk spectra at low accretion rates $\dot{M} \ll \dot{M}_{\mathrm{Edd}}$,

- Self-obscuration and obscuration by debris are present in the system. Self-obscuration leads to softer spectrum while obscuration by debris may make a fallback disk invisible during most of the active accretion period.

- The GW signal depends weakly on the orientation of the spin. The GW burst will be challenging to be detected for extragalactic sources.

8. ACKNOWLEDGEMENTS

REFERENCES

Abramowicz, M. A., Czerny, B., Lasota, J. P., & Szuszkiewicz, E. 1988, Ap. J., 332, 646

Alcubierre, M. 2008, Introduction to 3+1 numerical relativity (Oxford: Oxford University Press)

Ansorg, M., Brügmann, B., & Tichy, W. 2004, Phys. Rev. D, 70, 064011

Baiotti, L., Hawke, I., Montero, P. J., Löffler, F., Stergioulas, N., Rezzolla, L., Font, J. A., & Seidel, E. 2005, Phys. Rev., D71, 024035

Baker, J. G., Centrella, J., Choi, D.-I., Koppitz, M., & van Meter, J. 2006, Phys. Rev. Lett., 96, 111102

Bardeen, J. M., & Petterson, J. A. 1975, Astrophys.J., 195, L65

Bardeen, J. M., Press, W. H., & Teukolsky, S. A. 1972, Ap. J., 178, 347

Baumgardt, H., Makino, J., & Ebisuzaki, T. 2004, Ap. J., 613, 1143

Baumgarte, T. W., & Shapiro, S. L. 2010, Numerical Relativity: Solving Einstein's Equations on the Computer (Cambridge University Press)

Begelman, M. C. 2001, Ap. J., 643, 1065

Blandford, R. D., & Payne, D. G. 1982, MNRAS, 199, 883

Bode, T., Bogdanovic, T., Haas, R., Healy, J., Laguna, P., & Shoemaker, D. 2011, ArXiv e-prints

Bode, T., Shoemaker, D., Herrmann, F., & Hinder, I. 2008, Phys. Rev. D, 77, 044027

Bode, T., et al. 2009, Phys. Rev., D80, 024008

Bogdanović, T., Eracleous, M., Mahadevan, S., Sigurdsson, S., & Laguna, P. 2004, Ap. J., 610, 707

Bowen, J. M., & York, Jr., J. W. 1980, Phys. Rev. D, 21, 2047

Campanelli, M., Lousto, C. O., Marronetti, P., & Zlochower, Y. 2006, Phys. Rev. Lett., 96, 111101

Cannizzo, J. K., Lee, H. M., & Goodman, J. 1990, Ap. J., 351, 38

Carter, B., & Luminet, J. P. 1982, Nature, 296, 211

Clausen, D., & Eracleous, M. 2011, Ap. J., 726, 34

Conconi, P., Campana, S., Tagliaferri, G., Pareschi, G., Citterio, O., Cotroneo, V., Proserpio, L., & Civitani, M. 2010, MNRAS, 405, 877

Czerny, B., & Elvis, M. 1987, Ap. J., 321, 305

Davis, S. W., Narayan, R., Zhu, Y., Barret, D., Farrell, S. A., Godet, O., Servillat, M., & Webb, N. A. 2011, ApJ, 734, 111

Done, C., & Davis, S. W. 2008, Ap. J., 683, 389

Donley, J. L., Brandt, W. N., Eracleous, M., & Boller, T. 2002, AJ, 124, 1308

Dotan, C., & Shaviv, N. J. 2011, MNRAS, 413, 1623

Dursi, L. J., & Timmes, F. X. 2006, Astrophys. J., 641, 1071

Eddington, A. S. 1926, The Internal Constitution of the Stars (Cambridge: Cambridge University Press)

EinsteinToolkit. 2011, Einstein Toolkit: Open software for relativistic astrophysics

Esquej, P., Saxton, R. D., Freyberg, M. J., Read, A. M., Altieri, B., Sanchez-Portal, M., & Hasinger, G. 2007, A&A, 462, L49

Evans, C. R., Iben, I., & Smarr, L. 1987, Astrophys.J., 323, 129

Evans, C. R., & Kochanek, C. S. 1989, Ap. J., 346, L13

Farrell, S., Webb, N., Barret, D., Godet, O., & Rodrigues, J. 2009, Nature, 460, 73

Fragile, P. C., Blaes, O. M., Anninos, P., & Salmonson, J. D. 2007, Ap. J., 668, 417

Gerssen, J., van der Marel, R. P., Gebhardt, K., Guhathakurta, P., Peterson, R. C., & Pryor, C. 2002, AJ, 124, 3270

Gezari, S. 2010, in IAU Symposium, Vol. 267, IAU Symposium, 319–324

Gould, A. 2011, ApJ, 729, L23+

Guillochon, J., Ramirez-Ruiz, E., Rosswog, S., & Kasen, D. 2009, Ap. J., 705, 844

Hamada, T., & Salpeter, E. E. 1961, ApJ, 134, 683

Harris, W. E. 1991, ARA&A, 29, 543

Henke, B. L., Gullikson, E. M., & Davis, J. C. 1993, Atomic Data and Nuclear Data Tables, 54, 181

Herrmann, F., Hinder, I., Shoemaker, D., & Laguna, P. 2007a, Classical and Quantum Gravity, 24, 33

Herrmann, F., Hinder, I., Shoemaker, D., Laguna, P., & Matzner, R. A. 2007b, Ap. J., 661, 430

Hinder, I., Vaishnav, B., Herrmann, F., Shoemaker, D. M., & Laguna, P. 2008, Phys. Rev. D, 77, 081502

Husa, S., Hinder, I., & Lechner, C. 2006, Computer Physics Communications, 174, 983

Irwin, J. A., Brink, T. G., Bregman, J. N., & Roberts, T. P. 2010, ApJ, 712, L1

Kasen, D., & Ramirez-Ruiz, E. 2009, Ap. J., 714, 155

Katz, B., Budnik, R., & Waxman, E. 2010, Astrophys. J., 716, 781

Kawaguchi, T. 2003, Ap. J., 593, 69

Kesden, M. 2011, ArXiv e-prints

Kobayashi, S., Laguna, P., Phinney, E. S., & Meszaros, P. 2004, Astrophys. J., 615, 855

Komatsu, E., et al. 2011, ApJS, 192, 18

Krolik, J. H., & Piran, T. 2011, astro-ph/1106.0923

Laguna, P., Miller, W. A., & Zurek, W. H. 1993a, Ap. J., 404, 678

Laguna, P., Miller, W. A., Zurek, W. H., & Davies, M. B. 1993b, Ap. J. Lett., 410, L83

Lasota, J. P. 1994, in NATO ASI Series C, Vol. 417, Theory of Accretion Disks, ed. W. J. D. et al., Garching, 341

Lee, W. H., Ramirez-Ruiz, E., & Page, D. 2005, Astrophys.J., 632, 421

LIGO Scientific Collaboration. 2009

Lodato, G., King, A. R., & Pringle, J. E. 2009, Monthly Notices of the Royal Astronomical Society, 392, 332

Loeb, A., & Ulmer, A. 1997, Ap. J., 489, 573

Löffler, F., Rezzolla, L., & Ansorg, M. 2006, Phys. Rev. D, 74, 104018

Luminet, J.-P. 1985, Annales de Physique, 10, 101

Luminet, J.-P., & Marck, J.-A. 1985, MNRAS, 212, 57

Luminet, J.-P., & Pichon, B. 1989, A&A, 209, 85

Magorrian, J., & Tremaine, S. 1999, MNRAS, 309, 447

Mazzitelli, I., & Dantona, F. 1986, Ap. J., 311, 762

McClintock, J. E., et al. 2011, Classical and Quantum Gravity, 28, 114009

McLaughlin, D. E. 1999, AJ, 117, 2398

Merritt, D., & Poon, M. Y. 2004, ApJ, 606, 788

Mukai, K. 1993, Legacy, vol. 3, p.21-31, 3, 21

Nauenberg, M. 1972, ApJ, 175, 417

Oppenheimer, J., & Volkoff, G. 1939, Phys.Rev., 55, 374

Owocki, S. P., & Gayley, K. G. 1997, ASP Conf. Proc., 120, 121

Papaloizou, J. C. B., & Pringle, J. E. 1983, MNRAS, 202, 1181

Phinney, E. S. 1989, in IAU Symposium, Vol. 136, The Center of the Galaxy, ed. M. Morris, 543–+

Rees, M. J. 1988, Nature, 333, 523

Reid, I. N. 2005, ARA&A, 43, 247

Rosswog, S., Ramirez-Ruiz, E., & Hix, R. 2009, Astrophys. J., 695, 404

Rybicki, G. B., & Lightman, A. P. 1979, Radiative Processes in Astrophysics (New York: Wiley)

Sadowski, A. 2009, Ap. J. Supp., 183, 171

Sakimoto, P. J., & Coroniti, F. V. 1981, Ap. J., 247, 19

Schnetter, E., Hawley, S. H., & Hawke, I. 2004, Class. Quant. Grav., 21, 1465

Sesana, A., Vecchio, A., Eracleous, M., & Sigurdsson, S. 2008, MNRAS, 391, 718

Shakura, N. I., & Sunyaev, R. A. 1973, Astron. and Astrophys., 24, 337

Shapiro, S. L., & Teukolsky, S. A. 1986, Black Holes, White Dwarfs and Neutron Stars: The Physics of Compact Objects (Wiley: New York)

Shaviv, N. J. 2001, MNRAS, 326, 126

Stone, N., & Loeb, A. 2011, ArXiv e-prints

Strubbe, L. E., & Quataert, E. 2009, MNRAS, 400, 2070

Thornburg, J. 2004, Class. Quant. Grav., 21, 743

Tolman, R. C. 1939, Phys.Rev., 55, 364

Tundo, E., Bernardi, M., Hyde, J. B., Sheth, R. K., & Pizzella, A. 2007, ApJ, 663, 53

Ulmer, A., Paczynski, B., & Goodman, J. 1998, Astron. and Astroph., 333, 379

Vaishnav, B., Hinder, I., Herrmann, F., & Shoemaker, D. 2007, Phys. Rev., D76, 084020

Voges, W., et al. 2000, IAU Circ., 7432, 1

Wang, J., & Merritt, D. 2004, Ap. J., 600, 149

York, J. W. 1979, in Sources of Gravitational Radiation, ed. L. L. Smarr (Cambridge, UK: Cambridge University Press), 83–126